JACS
JOURNAL OF THE AMERICAN CHEMICAL SOCIETY
pubs.acs.org/JACS
Article

Noncovalent Peptide Assembly Enables Crystalline, Permutable, and Reactive Thiol Frameworks

Selina S. Hess, Francesco Coppola, Viet Thuc Dang, Phuong Nguyen Tran, Philip J. Mickel, Julia Oktawiec, Zhong Ren, Petr Král, and Andy I. Nguyen*

Cite This: J. Am. Chem. Soc. 2023, 145, 19588−19600
Read Online

ABSTRACT: Though thiols are exceptionally versatile, their high reactivity has also hindered the synthesis and characterization of well-defined thiol-containing porous materials. Leveraging the mild conditions of the noncovalent peptide assembly, we readily synthesized and characterized a number of frameworks with thiols displayed at many unique positions and in several permutations. Importantly, nearly all assemblies were structurally determined using single-crystal X-ray diffraction to reveal their rich sequence−structure landscape and the cooperative noncovalent interactions underlying their assembly. These observations and supporting molecular dynamics calculations enabled rational engineering by the positive and negative design of noncovalent interactions. Furthermore, the thiol-containing frameworks undergo diverse single-crystal-to-single-crystal reactions, including toxic metal ion coordination (e.g., Cd^{2+}, Pb^{2+}, and Hg^{2+}), selective uptake of Hg^{2+} ions, and redox transformations. Notably, we find a framework that supports thiol−nitrosothiol interconversion, which is applicable for biocompatible nitric oxide delivery. The modularity, ease of synthesis, functionality, and well-defined nature of these peptide-based thiol frameworks are expected to accelerate the design of complex materials with reactive active sites.

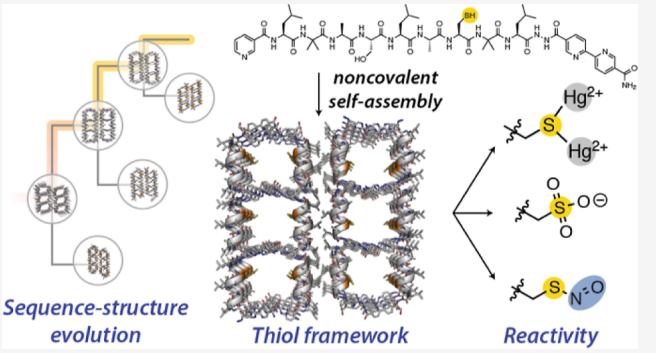

INTRODUCTION

Peptides have expanded the structural−functional space of materials[1−4] due to their remarkable modularity and high-yielding generalized synthesis.[5,6] In addition to the myriad of 1D and 2D peptide-based assemblies, recent developments have enabled the synthesis of structurally defined 3D extended assemblies (or frameworks) from small peptides[4,7−12] that possess channels or pores capable of engaging with exogenous substrates, demonstrating how minimalist building blocks can mimic the protein active sites. Materials derived from peptides can display advanced bioinspired functionalities owing to the chirality,[11,13,14] permutability,[12] and conformational flexibility[7,12,15,16] of the building blocks. Furthermore, unlike metal−organic and covalent organic frameworks (MOFs and COFs, respectively), peptides assemble under mild conditions due to the usage of weak but numerous noncovalent and shape-specific interactions,[17−19] allowing for new strategies to generate materials tolerant of more reactive moieties.

Thiols are potent nucleophiles,[20] redox-active,[21−23] and capable of undergoing a variety of reversible reactions,[24] making their incorporation into porous materials of significant interest (Figure 1). The high affinity of thiols toward soft metal cations (e.g., Hg^{2+})[25] could enable the design of solid-state adsorbents for these toxic contaminants or valuable resources. In biology, the thiol group of cysteine plays several key roles in the active sites of notable enzymes (e.g., proteases,[26] ribonucleotide reductase,[27] and thioredoxin[28]), metalloproteins (e.g. iron−sulfur cluster proteins,[29] blue copper proteins,[30] metallothionein,[31] and cytochrome P450s[32,33]), and redox switches capable of sensing reactive oxygen,[22] nitrogen,[34] and electrophilic species;[35] hence, access to thiol-containing frameworks could greatly advance the development of biomimetic materials. Lastly, thiols are efficiently and orthogonally transformed into other useful moieties by conjugation with olefins,[36] Michael acceptors,[37] alkyl/aryl halides,[38] and disulfides,[24] rendering materials possessing thiols adaptable and tunable.

However, the high reactivity and sensitivity of thiols have made them particularly challenging to directly incorporate into ordered porous materials like MOFs and COFs, both of which generally utilize components that also react with thiols (Figure 1). Thus, most methods to produce thiol-containing pores rely on the postsynthetic modifications of MOFs[39−43] or COFs[44−46] that graft thiol units randomly or incompletely throughout the

Received: April 7, 2023
Published: August 28, 2023

https://doi.org/10.1021/jacs.3c03645
J. Am. Chem. Soc. 2023, 145, 19588−19600

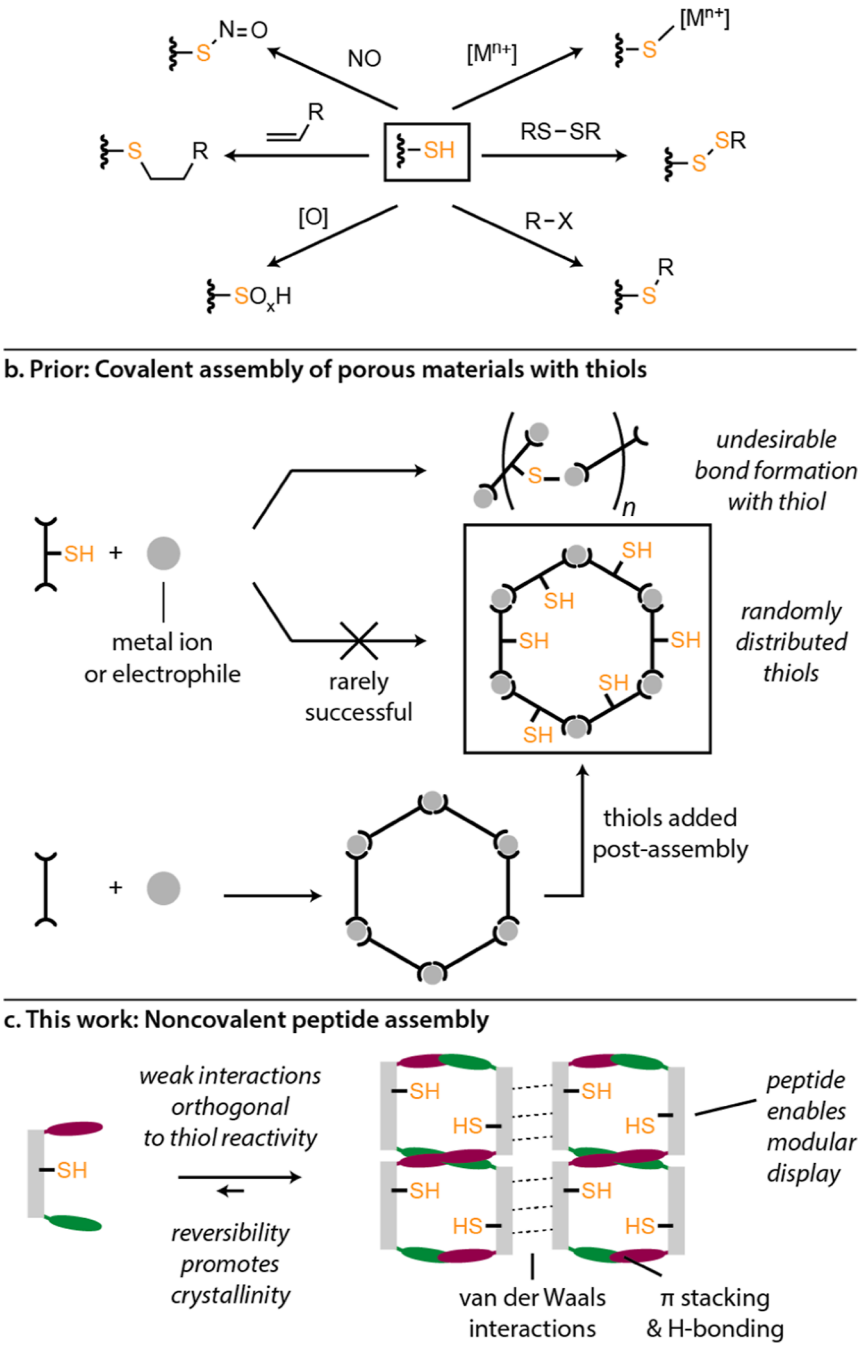

Figure 1. (a) Chemical versatility of the thiol unit. (b) Generalized strategy to synthesize thiol-containing frameworks. (c) Noncovalent peptide assembly to create crystalline thiol-containing peptide frameworks.

materials.[39,47] Zr-based MOFs are the only demonstrated class that can directly use thiol-containing ligands in their synthesis, though there are very few examples, and the thiols are typically randomly positioned.[48−50] Consequently, the less-defined nature of these previous examples has prevented thorough structural characterization, especially by single-crystal X-ray diffraction (SC-XRD), which has resulted in an incomplete understanding of their structure−function relationships. Overall, the limited strategies to incorporate thiols into framework materials and the lack of structural data impede the rational engineering of their function.

To address the aforementioned challenges, we employ a noncovalent peptide-π-stack assembly strategy developed in this laboratory.[12] This strategy uses shape-specific van der Waals, H-bonding, and $\pi-\pi$ interactions encoded by a peptide sequence to control the framework synthesis. Since the peptide framework assembly relies on weak interactions from the less reactive functional groups, we hypothesize that this approach will tolerate the presence of reactive thiol groups during the assembly process to provide a novel and convenient route toward well-defined thiol-containing materials (Figure 1).

RESULTS AND DISCUSSION

Exploration of Sequence−Structure Relationships. To begin, we used **UIC-1** as a starting point for engineering in thiol groups. As a summary, **UIC-1** is a nine amino acid sequence capped with bipyridyl moieties that assembles into a lattice with

https://doi.org/10.1021/jacs.3c03645
J. Am. Chem. Soc. 2023, 145, 19588−19600

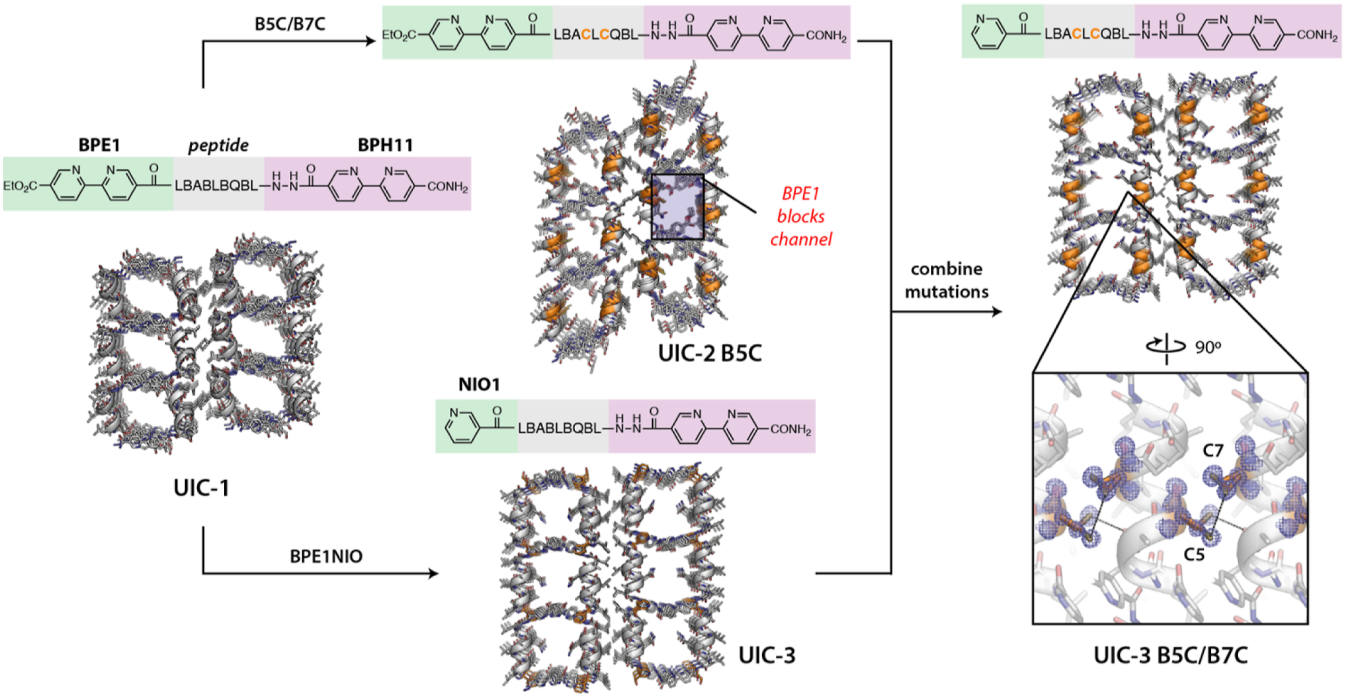

Figure 2. Mutation of BPE1 of BPE1 to NIO1 enables porous frameworks with thiol display. X-ray crystal structures of **UIC-1**, **UIC-2 B5C**, **UIC-3**, and **UIC-3 B5C/B7C**. Inset shows Cys residues, each of which are disordered over two positions. $2F_o - F_c$ map at 1.0 σ around C5 and C7. Black lines indicate H bonds.

infinite rectangular channels and pore widths of ~11 × 15 Å (Figure 2).[12] We have previously shown that **UIC-1** is stable and functional as a sorbent in water and various organic solvents at ambient temperatures. The main design elements of **UIC-1** are α-helix-supporting aminoisobutyric acid (three-letter code Aib and one-letter code B) residues, a hydrophobic Leu-rich surface, and π-stacking bipyridyl residues (abbreviated with three-letter codes BPE and BPH, with BPH also containing a hydrazide moiety, Figure 2). **UIC-1** tolerates variations of positions 4, 5, and 7 to many residues including those that possess Lewis acidic and basic functionalities. Initial models based on the crystal structure of **UIC-1** suggested that a B7C mutation could allow the display of a thiol functionality in the main channel, and additionally, a double Cys mutation at 5 and 7 could potentially generate a bidentate metal-binding site. Based on these initial simulations, we synthesized these two variants by solid-phase peptide synthesis (SPPS) with mutations B7C and B5C/B7C, respectively.

Slow cooling from 80 °C of a saturated solution (Table S18) under N_2 atmosphere (to prevent the formation of disulfide bonds) produced single crystals of these two variants. Unexpectedly, SC-XRD of both revealed a similar arrangement of the peptides into an architecture less porous than that of **UIC-1**. We name the sequence possessing the B7C mutation associated with this new phase, **UIC-2**, and the doubly-mutated variant will be referred to as **UIC-2 B5C**. Henceforth, the mutated sequence that gives rise to a new phase will be renamed by increasing the numeric suffix of its parent's name (e.g., **UIC-1** to **UIC-2**), and further mutations that preserve the phase will be in reference to that renamed sequence (e.g., **UIC-2 B5C**).

In the **UIC-2** phase, peptides are arranged in a similar manner as in **UIC-1**, with a double layer of peptides held by a hydrophobic Leu interface and further interconnected through the $\pi-\pi$ stacking of BPH and BPE. However, all chains fold into a pure α-helix rather than the mixed 3_{10}-α fold seen in **UIC-1**. This alternate fold makes the BPH and BPE moieties no longer parallel to each other. Consequently, the pyridyl rings of BPE are significantly shifted into the pore space and reduce the size of the channel (widths of 4.6 × 4.6 Å, measured from BPE H161 to C7 Hγ and BPE H181 to BPE H191, respectively). The switch from mixed 3_{10}-α in **UIC-1** to pure α-helix in **UIC-2** is driven by an interchain H bond between C7 with a neighboring Q8 (S···O distance of 3.4 Å) that eliminates the key intermolecular Q8-B5 H bond that had stabilized the mixed 3_{10}-α fold. The breakage of the Q8-B5 H bond also occurs when **UIC-1** undergoes a B7H mutation (**UIC-2 C7H**), suggesting that the H-bonding residues at position 7 could significantly influence the self-assembly.

To remedy the decreased porosity of **UIC-2**-type frameworks, we hypothesized that changing the BPE of **UIC-1** to a single pyridyl ring, such as niacin (three-letter code NIO), would reopen the channel (Figure 2). Surprisingly, SC-XRD revealed a completely new framework with chevron-shaped pores, **UIC-3**. Similar to **UIC-1** and **UIC-2**, **UIC-3** contains double-layered peptide walls, and π-stacking from BPH and NIO generates infinite channels (widths of 13.3 × 11.0 Å, measured from BPH H181 to BPH H041 and Q8 Hβ to B7 Hβ, respectively) (Figure 2). Unlike previous frameworks, however, **UIC-3** has parallel orientations of helices across the channel, and the rungs of the π-stack are composed of a planar unit of H-bonded NIO and BPH residues joined by the pyridyl lone pair of NIO and the carboxamide of BPH. Although the intended **UIC-2**-type framework did not form upon the BPE1NIO mutation, **UIC-3** nonetheless possesses desirable large pores suitable for further exploration.

Applying the previously attempted B5C/B7C double mutation onto **UIC-3** succeeded in the preservation of the parent phase (thus, it is named **UIC-3 B5C/B7C**), enabling the display of two thiols per peptide in the channel, as determined by SC-XRD (Figure 2). C7 points directly into the pore space, but C5 is directed more toward the helix−helix interface and is able

https://doi.org/10.1021/jacs.3c03645
J. Am. Chem. Soc. 2023, 145, 19588−19600

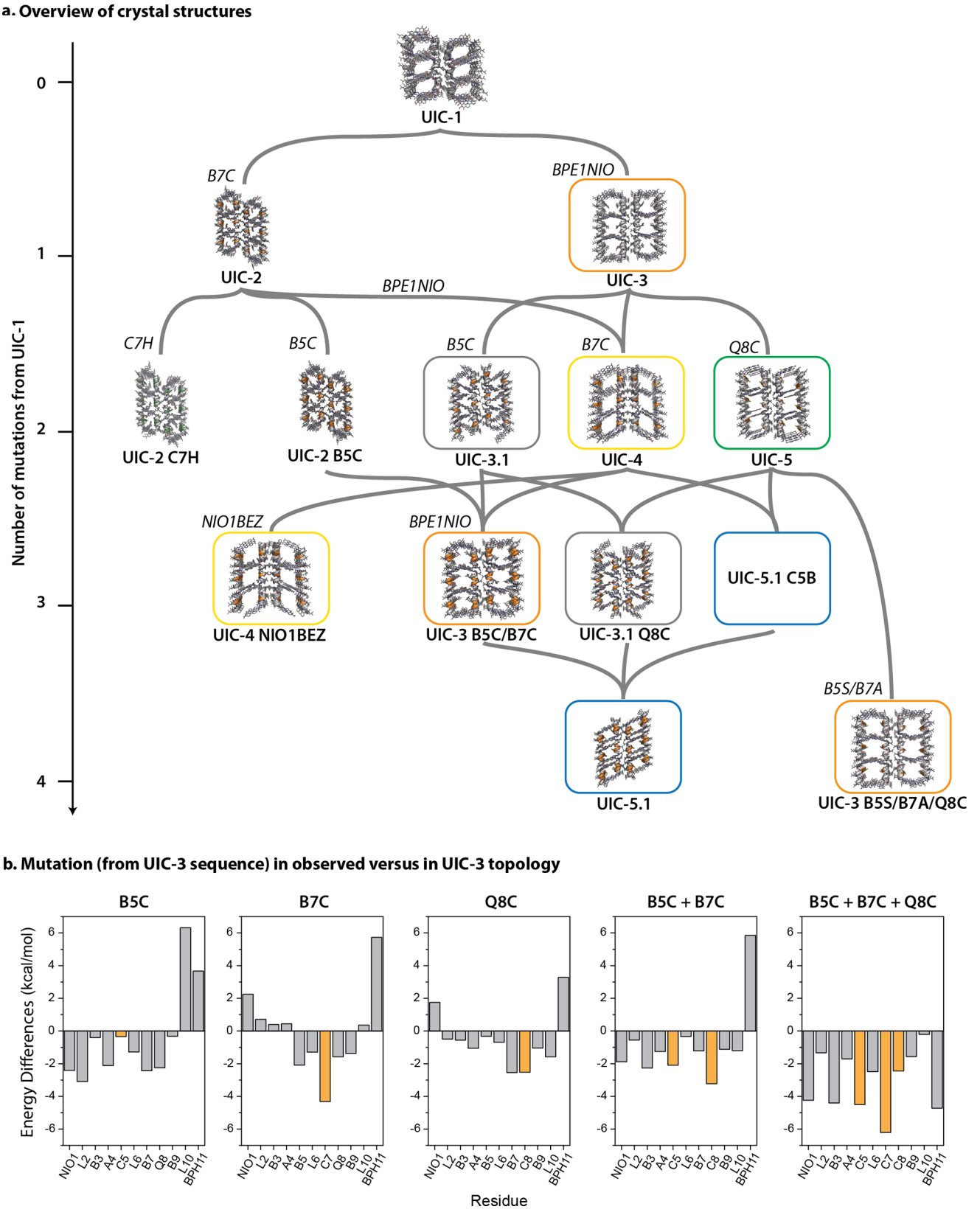

Figure 3. (a) Phylogenetic network showing relationships between frameworks. Each line connecting the SC-XRD structures represents mutations relating the sequences, and the vertical distance between nodes denotes the number of mutations introduced. Crystal structures with the same-colored boxes have identical topologies. (b) Energetic differences between the mutated sequence existing in the observed framework phase vs that if it were forced in the **UIC-3**-type phase. For consistency, all mutations are relative to the **UIC-3** sequence. Negative values are stabilizing.

to form a H bond either with a neighboring B3 (S···O distance of 3.2 Å) or with the sulfur of a neighboring C7 (S···S distance of

https://doi.org/10.1021/jacs.3c03645
J. Am. Chem. Soc. 2023, 145, 19588−19600

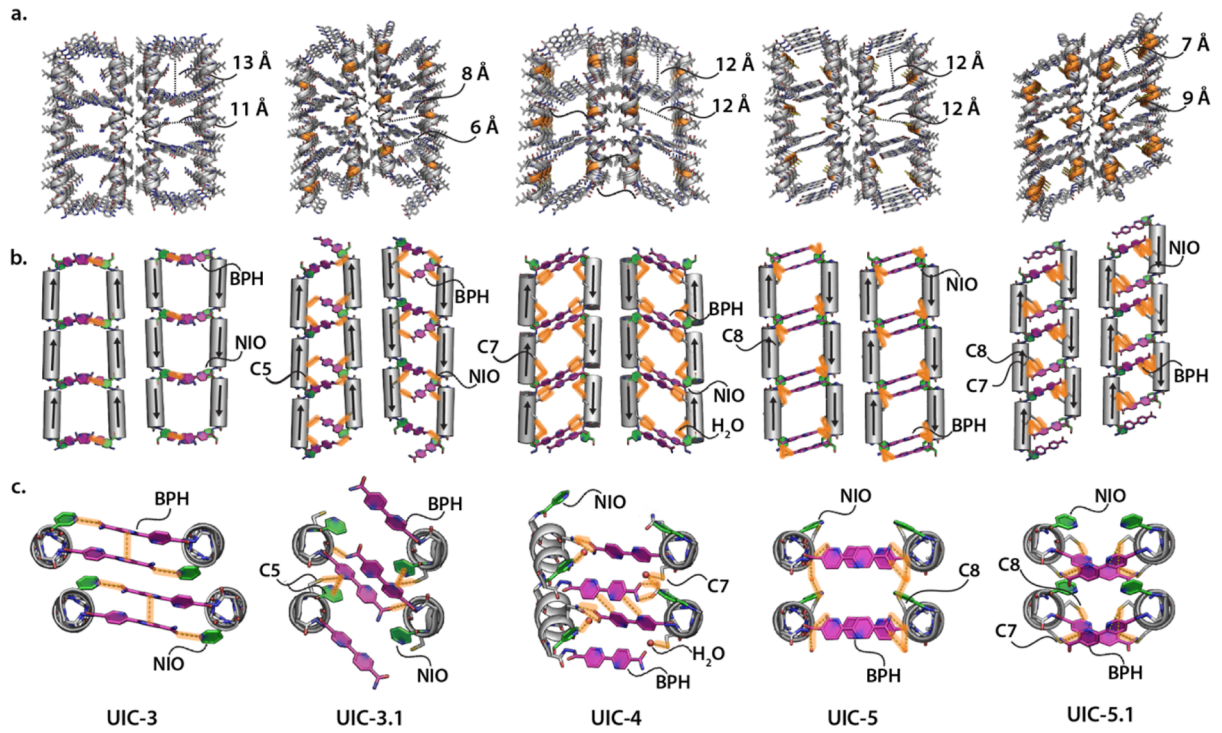

Figure 4. SC-XRD structures of the five different framework archetypes. (a) Representative portion of the crystalline lattice, with the measured pore widths indicated by dashed lines. Cys positions are highlighted in orange. (b) Simplified representations of the frameworks highlighting π-stacking aromatic residues (BPH and NIO, purple and green, respectively) and key H-bonding interactions. Arrows denote the direction of the peptide from the N- to C-terminus. (c) Top view perpendicular to the channel axis of the frameworks.

3.3 Å). Importantly, it is the first porous material to show the precise arrangement of thiols, which is crucial for rational engineering and structure−function analysis.

Given the success of the double Cys variant, **UIC-3 B5C/B7C**, in displaying thiol groups in the pore while retaining the **UIC-3** topology, we systematically examined single Cys mutations at positions 5, 7, and 8, which are all positions with side chains that could point into the channel (Figure 3a). Figures 4 and 5 more closely highlight the structural differences between the frameworks formed from each examined sequence. Surprisingly, the single Cys mutants of **UIC-3** created different framework phases from the double mutant **UIC-3 B5C/B7C**, implicating strong epistasis, where the effects of combined mutations behave very differently than what would be expected from the additive properties of its constituent mutations. As will be discussed below, the different locations of Cys lead to unique H-bond pairings that dictate the structure.

The B5C mutation to **UIC-3** generates a framework with peptide orientations (Figures 3a and 4) identical to that of **UIC-3** but is altered by slippage along the *a*-direction. Given the same peptide orientations and simple structural relationship between this framework and **UIC-3**, we name this sequence, **UIC-3.1**. Due to the slippage seen in **UIC-3.1**, the original pore of **UIC-3** becomes divided into two smaller channels having triangular cross sections (widths of 4.7 × 5.8 Å, measured from BPH11 H061 to BPH11 H051 and BPH11 H181 to A7 Hβ, respectively, and 4.5 × 8.4 Å, measured from Q8 Nε to BPH H011 and A4 Hβ to NIO H5, respectively). In **UIC-3.1**, a new H bond donation from C5 pulls BPH11 on a neighboring chain by ∼0.3 Å away from its position in **UIC-3**. This movement cascades into the breakage of the original H bond between BPH11 and NIO1, forming a new H bond between BPH11 and the carbonyl of A4 in chain A and a new H bond between BPH11 and the hydrazide of another BPH11 in chain B. Notably, the rearrangement of H-bonding partners results in a loss of continuous $\pi-\pi$ stacking rows that are characteristic of **UIC-1**, **UIC-2**, and **UIC-3**. There are isolated $\pi-\pi$ interactions between BPH11 and NIO1 (3.6 Å), but the closest BPH−BPH ring-to-ring distance along the channel direction (*b* axis) is 7.0 Å. A H bond between the NIO1 lone pair and hydrazide is also formed via a water molecule, further stabilizing the lattice. Overall, the introduction of C5 provides new H-bonding opportunities that lead to another framework phase.

The structure of the B7C mutant revealed a framework with parallelogram-shaped channels with antiparallel helical arrangement across the pore (widths of 10.4 × 11.7 Å, measured from BPH11 H181 to BPH11 H181 and C7 Hβ to C7 Hβ, respectively). Given this variant's drastic deviation in the helix orientation relative to **UIC-3**, we call this topology **UIC-4**. The introduced C7 residue engages in a H-bond network with the pyridyl N of NIO1 via a bridging water molecule that breaks the original NIO1−BPH11 H bond of **UIC-3**, likely accounting for the new topology. The displaced BPH11 now engages in H bonding with Q8 to form multivalent H bonds between both carboxamide moieties. These changes manifest in a looser $\pi-\pi$ stacking of the BPHs, with a ring-to-ring distance of 4.5 Å. If NIO is substituted for an isosteric but non-H-bonding analogue, benzoyl (BEZ), neither C7 nor BPH11 can make H bonds with this residue. We find that the NIO1BEZ mutation in **UIC-4** (Figure 3a) preserves the framework phase, showing that the C7−H_2O−NIO1 H-bond network is, in and of itself, not critical for maintaining the **UIC-4** topology.

In the Q8C mutation of **UIC-3**, C8 participates in the interchain H-bonding networks with NIO1 and BPH11 via one water molecule. Again, disruption of the NIO1-BPH11 H bond characteristic of **UIC-3** by the new Cys residue yields a new

https://doi.org/10.1021/jacs.3c03645
J. Am. Chem. Soc. 2023, 145, 19588−19600

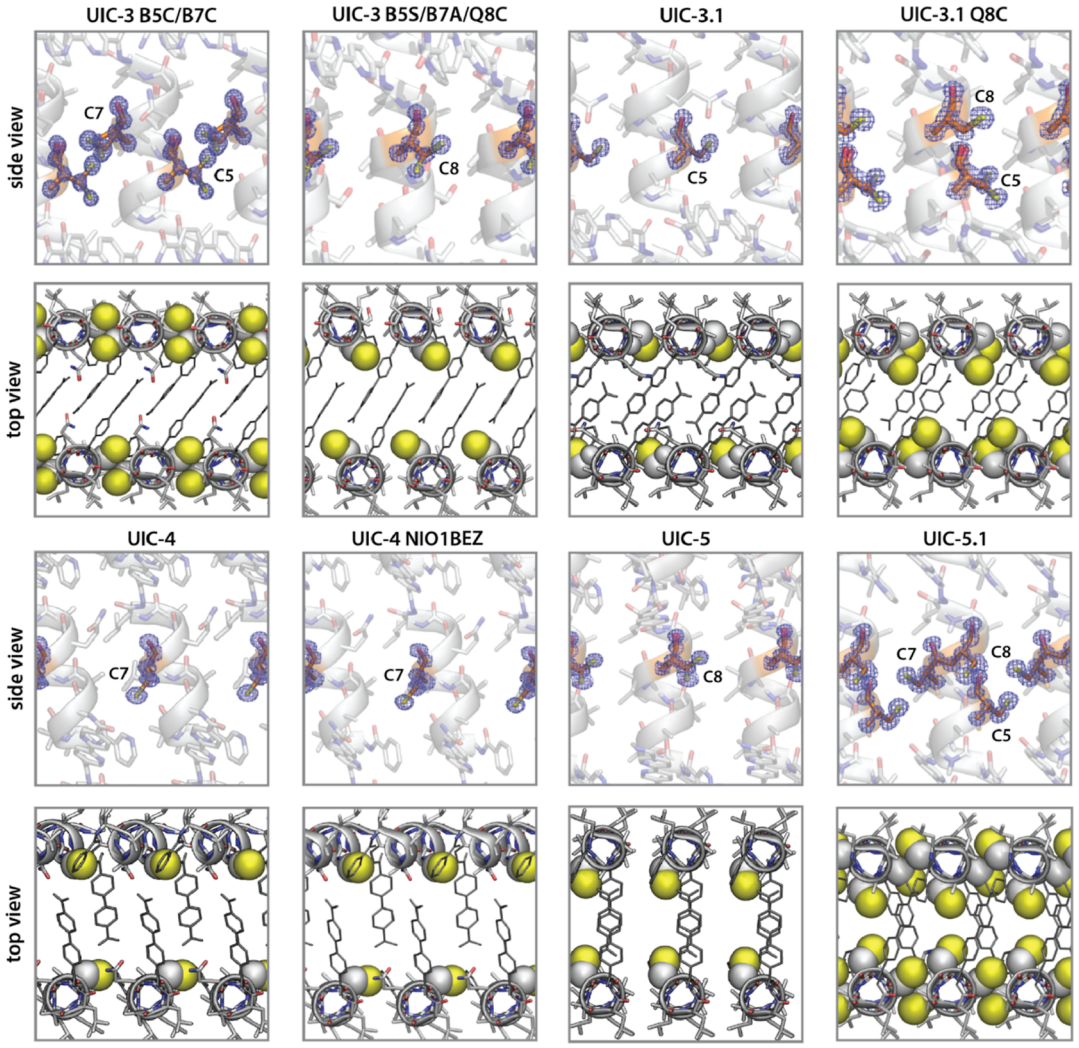

Figure 5. Side and top pore views perpendicular to the infinite channel axis for all Cys-containing frameworks with SC-XRD data. Cys residues in the side views are overlaid with their respective $2F_o - F_c$ map at 1.0 σ to show all the conformations of the side chain. Note that two Cys side chain rotamers exist in **UIC-3 B5C/B7C**, **UIC-3 B5S/B7A/Q8C**, **UIC 3.1**, and **UIC-5**. Cys residues in the top view are represented with van der Waals spheres (S is yellow, and C is gray), with only the major rotameric state shown (for clarity).

architecture. The channel is nearly square (widths of 11.5 × 12.1 Å, measured from C8 Hβ to A4 Hβ and BPH11 N17 to BPH11 H181, respectively). Across the channel, helices are arranged in an antiparallel fashion like in **UIC-4**, but unlike **UIC-4**, the coiled-coil packing within the walls is antiparallel (Figure 4), and so this framework is distinguished as **UIC-5**. New H-bond patterns are seen in **UIC-5**, with the BPH-carboxamide now H-bonding simultaneously with the hydrazide of BPH11 and carbonyl of C8. Interestingly, the BPH residues now form discrete $\pi-\pi$ stacking pairs (ring−ring distance of 3.8 Å) with large gaps between each pair (6.9 Å) resulting in an orthogonal channel along the *a*-axis.

As stated earlier, the Cys mutations are strongly epistatic, as the structures of the single mutations of **UIC-3** do not resemble that of the double B5C/B7C mutation. To further explore the extent of epistasis, we examined all other possible simultaneous variations in addition to B5C/B7C: B5C/Q8C, B7C/Q8C, and the triple mutation B5C/B7C/Q8C. SC-XRD structures were obtained for all, except B7C/Q8C, for which only a powder XRD pattern was obtainable (Figure S31). The double B5C/Q8C mutant has essentially identical peptide arrangements, pore shapes, and H-bonding patterns to **UIC-3.1**, and hence, we name this **UIC-3.1 Q8C**.

The triple B5C/B7C/Q8C mutation forms a slipped version of **UIC-5**, and thus, we name it **UIC-5.1**. The triple mutant also self-assembled into an antiparallel coiled coil with, however, significantly smaller pores than those in **UIC-5** (widths of 7.2 × 8.7 Å, measured from NIO H5 to NIO H5 and C8 Hγ to C8 Hγ, respectively). In comparison to **UIC-5**, **UIC-5.1** has a significant slip along the *a*-direction due to a multivalent sulfur−aromatic interaction involving BPH11 with C7 and C8 (ring···S distances of 3.7 Å for both). C5 only H-bonds with the carbonyl group of the neighboring B3, very similar to what is seen in **UIC-3 B5C/B7C**.

Based on the insights derived from the previously described SC-XRD structures, the B7C/B8C double mutant (for which only a PXRD pattern was obtainable) is expected to form similar S−aromatic interactions as **UIC-5.1**. Rietveld refinement using **UIC-5.1** with a C5B mutation as a starting point yielded a satisfactory fit that suggests that the two variants have similar structures (Figure S31).

Molecular Dynamics. To understand the energetic basis for why certain mutations lead to phase changes, we used classical

https://doi.org/10.1021/jacs.3c03645
J. Am. Chem. Soc. 2023, 145, 19588−19600

atomistic molecular dynamics (MD) simulations to locate energy differences at each residue between the experimentally observed phase caused by the mutation and a hypothetical phase where the mutation is forced to exist in its parent phase. This allows us to quantify the stabilization gained when crystallizing in a different phase than that of its parent. For each framework, we calculated the interaction energies between each amino acid of a central peptide in a supercell and the rest of the lattice (Tables S25 and S26).

A series of comparisons were aimed at answering why introducing either single or certain multiple Cys mutations to **UIC-3** resulted in phase changes. Figure 3b shows the energy difference per residue between the observed phases and if that mutation was forced in the **UIC-3** phase. Consistent with the observations, the total energy of the peptide is always lower in the experimentally determined phase than that in the hypothetical phase. No single residue differed by more than 6.4 kcal/mol between the two compared phases, demonstrating that weak interactions shape the sequence−structure space.

Cys residues are consistently more stable in the observed structures, supporting the inference from SC-XRD structures that new phases are created from favorable interactions involving the thiol group. Interestingly, in all cases, the stabilization of Cys residues also triggers the destabilization or stabilization of many other positions that are not necessarily interacting with the thiol, demonstrating the cooperative energetics supporting the framework. Cooperativity is significant as it could permit the manipulation of the framework phases by targeting other residues besides Cys. Lastly, in phases other than that of **UIC-3**, BPH becomes destabilized in all, except for **UIC-5.1**, which may be explained by the lack of tightly packed π-stacking (Figure 4). BPH is perhaps more stable only in **UIC-5.1** because in that topology it is able to engage in two S···aromatic interactions with C7 and C8. Overall, MD calculations reinforce the conclusions derived from SC-XRD structures and show that weak energetic interactions (less than 6.4 kcal/mol residue) determine the resultant phases. The shallowness of the structure−energy surface may be important in allowing for the evolvability and adaptability of these peptide frameworks with simple mutations.

Rational Design. The introduction of thiol groups, which can engage in H-bonding and sulfur−aromatic interactions, competes with or disrupts previous H-bonding motifs and yields new topologies. In this context, it is interesting why **UIC-3 B5C/B7C** *did not* disrupt the **UIC-3** phase. In either the single B5C or B7C variant (**UIC-4** and **UIC-5**, respectively), the Cys residues form H bonds with various residues that destroyed the **UIC-3** topology, but combining both single mutations in **UIC-3 B5C/B7C** instead led to a C5−C7 H bond (S···S distance of 3.2 Å) that neutralizes their ability to engage with other functional groups (Figure 1). This suggests that the rational manipulation of H bonding could allow the desired Cys mutations to exist in the intended framework.

To test whether H bonds could be controlled rationally, we targeted a hypothetical **UIC-3**-type phase that could display a Cys in the eighth position. As discussed earlier, a sole Q8C mutation to **UIC-3** results in **UIC-5** instead. To disfavor the **UIC-5** topology, we identified a potential weak link in this phase: a H bond between the BPH carboxamide and a barely exposed N−H group on the hydrazido unit of an opposing chain (Figures 4 and 6). We hypothesized that mutations that could further obscure the hydrazide N−H group would disallow H bonding and therefore prevent the formation of the **UIC-5** phase

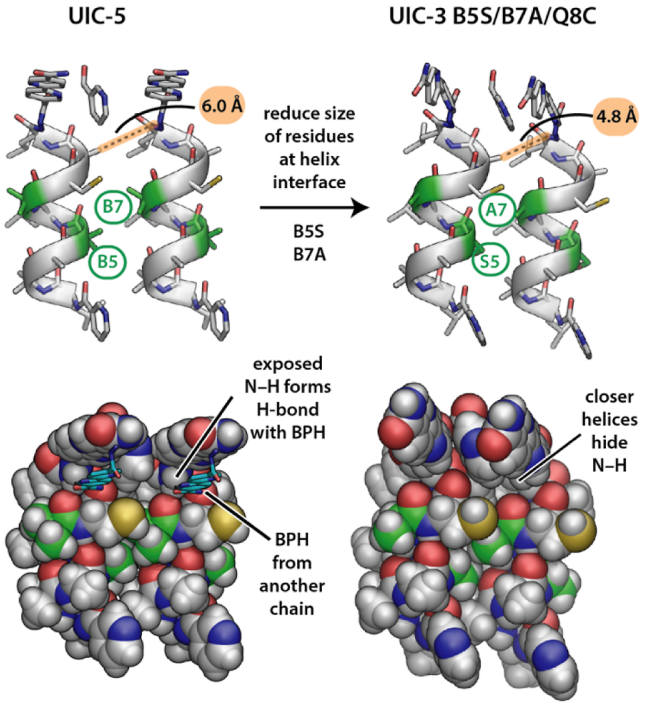

Figure 6. Rational design strategy to increase the steric hindrance around the N−H bond in the hydrazido moiety indicated to disfavor the **UIC-5**-type phase.

(Figure 6). Inspection of the **UIC-5** structure suggested that if the helix−helix distances along the *b*-axis were decreased, the hydrazide N−H group would become buried by the side chains of the neighboring helix. In order to allow closer packing of the helices, the bulky Aib residues at the helical interface, B7 and B5, were reduced to smaller residues, A7 and S5, respectively (we chose S5 because initially we expected it could favorably H-bond with the neighboring chain as is seen in **UIC-3 B5C/B7C**), and SC-XRD confirms that the introduction of B5S/B7A/Q8C mutations to **UIC-3** preserves the parent phase and displays C8 directly into the pore (this sequence is named **UIC-3 B5S/B7A/Q8C**, Figure 3a). The smaller residues allow bringing the methyl group of B9 by 1.2 Å closer to the hydrazide (C···N distance of 4.8 Å in **UIC-3 B5S/B7A/Q8C** vs 6.0 Å in **UIC-5**), which significantly increases the steric bulk around the N−H group and thus disfavors its involvement in H bonding. Unlike our intention, S5 did not H-bond with the neighboring chain, though it instead minimizes its extension by tucking inward via an intrachain H bond with the *i*−3 carbonyl oxygen. Overall, this example demonstrates the success of rational negative design, the introduction of elements that disfavor alternative assemblies, in the engineering of peptide frameworks. Furthermore, it also highlights that H-bond networks are cooperative, consistent with MD calculations (vide supra), and that they can collapse totally by eliminating only part of the network.

Thus far, the exploration of the sequence space and rational design created eight porous architectures with single, double, and triple display of thiol groups in the channel (Figure 5). These eight structures group into five families (Figure 4), providing diverse steric and electronic environments (Figure 5). These thiol groups are directly introduced during the assembly without the need of protecting the groups nor postsynthetic modifications, and, importantly, yield high-resolution crystal structures from which rational design principles were derived.

https://doi.org/10.1021/jacs.3c03645
J. Am. Chem. Soc. 2023, 145, 19588−19600

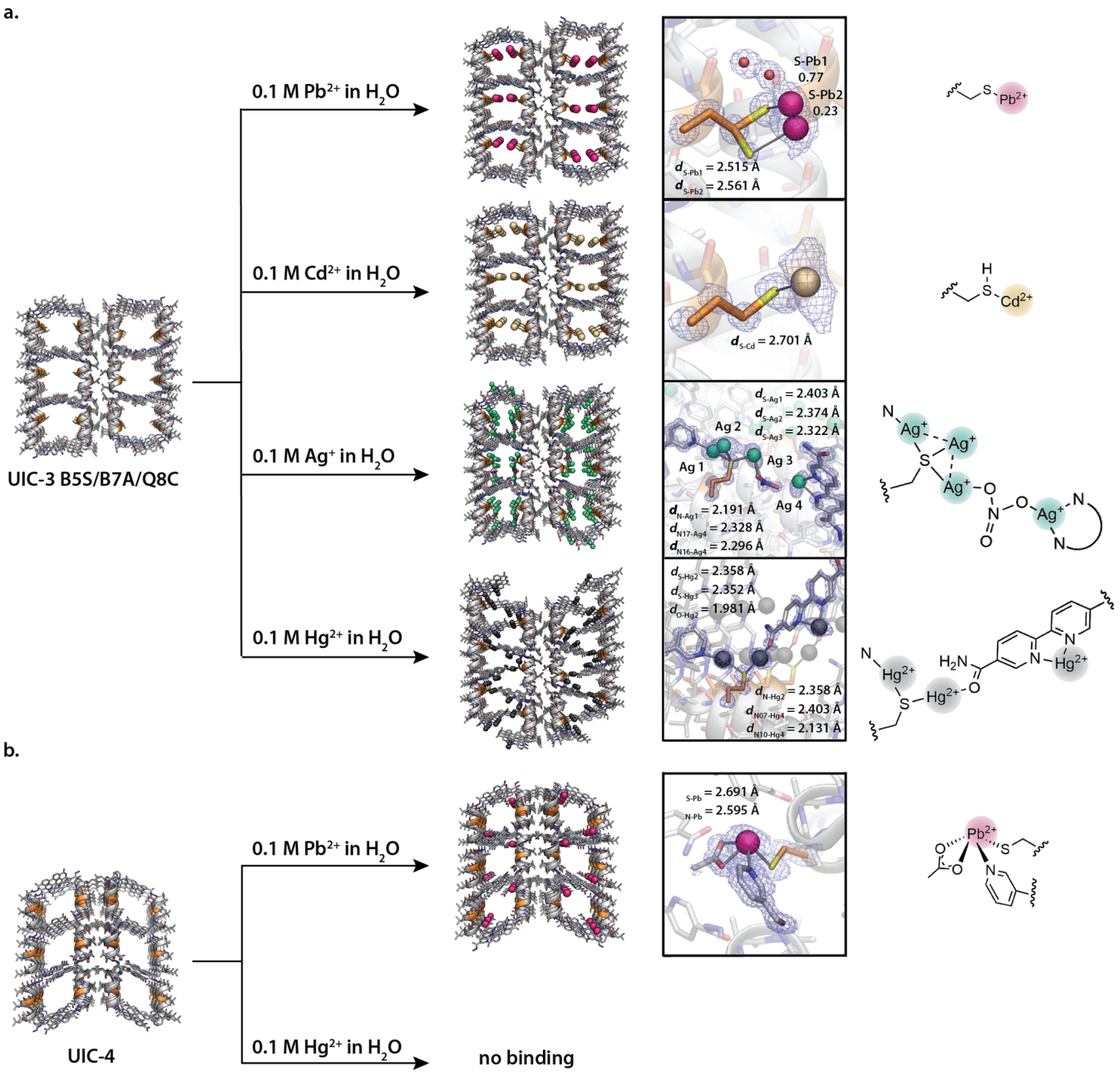

Figure 7. X-ray crystal structures from single-crystal-to-single-crystal metalation reactions of thiol-containing frameworks. The framework and close-up views are shown ($2F_o - F_c$ map at 1.0 σ). (a) Metallation of **UIC-3 B5S/B7A/Q8C**. Note the significant framework distortions observed upon Ag^+ and Hg^{2+} binding. (b) Selective Pb^{2+} binding by **UIC-4**, forming a hemidirected tetrahedral coordination geometry.

Reactivity with Metal Ions. Given the metal-binding ability of thiols, cysteine-containing mutants were exposed to various metal ions in aqueous solutions to examine the metal coordination capabilities of these porous frameworks and their potential ability to remove toxic ions from solution (Figure 7). According to the hard–soft acid–base (HSAB) theory,[25] thiols are soft bases with a high preference to bind soft acids such as Cd^{2+}, Pb^{2+}, Hg^{2+}, and Ag^+, many of which are severely toxic. Though previous reports[39−50] have shown that thiol-containing frameworks can capture these metal ions, there are no examples that have structurally characterized the binding by SC-XRD, resulting in an incomplete understanding of how framework structure impacts metal coordination chemistry. We began screening crystals for metal uptake by soaking single crystals of several thiol frameworks possessing larger pore widths (~10 Å) in aqueous solutions of $Pb(OAc)_2$ to analyze metal binding by SC-XRD. Interestingly, soaked crystals **UIC-3 B5C/B7C** (C5, C7), **UIC-5** (C8), and **UIC-5.1** (C5, C7, C8) show no electron density for Pb^{2+} by SC-XRD despite the high scattering cross section of Pb and the typically favorable Pb–S bond. Further inspection of these peptide frameworks shows that their steric environment around the Cys residue is crowded (Figure 5), likely inhibiting metal coordination.

However, **UIC-3 B5S/B7A/Q8C** (C8) and **UIC-4** (C7) show quantitative uptake of either Pb^{2+} or Cd^{2+} ions from 0.1 M solutions, with both structures showing a 1:1 stoichiometry of the peptide to metal. These are the first reported SC-XRD structures of metal binding to a thiol-containing framework. In **UIC-3 B5S/B7A/Q8C,** the Cys residues protrude further into the channel (Figure 5), providing ample space for metal

https://doi.org/10.1021/jacs.3c03645
J. Am. Chem. Soc. 2023, 145, 19588−19600

coordination. Pb^{2+} coordinates in a monodentate fashion to C8 and is disordered over two side-chain rotamers (77% χ1 = trans and 23% χ1 = gauche+).

Though the electron density for the disordered Pb is clear, it is difficult to pinpoint the positions of its coordinated waters and acetate counterions. The observed Pb···S distances of 2.52−2.56 Å suggest that Cys is deprotonated.[51] Cd^{2+} exhibits a Cd···S distance of 2.70 Å, typical of Cd^{2+} interactions with neutral sulfur donors, suggesting a protonated Cys.[52] Notably, neither Pb^{2+} nor Cd^{2+} coordinates to the bipyridyl moieties, which could be due to the weak σ-donor strength of BPH.[53]

A much higher metal uptake was obtained for $AgNO_3$ (Figure 7) by **UIC-3 B5S/B7A/Q8C** crystals. SC-XRD revealed a ratio of 4:1 between the Ag^+ ion and peptide. Three ions bind to the C8 side chain, forming an Ag_3-μ^3-S unit, and the remaining Ag^+ binds to the BPH nitrogen atoms in a bidentate fashion (Ag···N distance of 2.60 Å). Here, BPH and Ag^+ are disordered by a rotation ∼180° around the C12−C13 bond (occupancies of 71% and 29%). Ag2 binds to the Cys side chain in a monodentate mode (Ag···S distance of 2.38 Å), and Ag3 binds to the side chain as well as a nitrate counterion. The Ag_3-μ^3-S unit possesses Ag1···Ag2 and Ag2···Ag3 distances of 3.14 and 3.36 Å, indicating stabilizing argentophilic interactions within the cluster.[54] Significantly, Ag1 is bound in a bidentate fashion to the thiolate of C8 and NIO pyridyl N of a neighboring peptide (Ag···S distance of 2.40 Å and Ag···N distance of 2.19 Å), yielding a linear coordination geometry. The usage of NIO in Ag^+ coordination breaks the NIO1−BPH11 H bond in the archetypical **UIC-3** framework (vide supra), causing a significant distortion of the pore to a more exaggerated chevron shape. Interestingly, the distortion creates a new short C−H···O contact of 3.02 Å between C4 NIO and the carboxamide O of BPH, showcasing the non-negligible stabilization from weaker interactions.

Hg^{2+}, another highly thiophilic and extremely poisonous ion, also binds with multiple equivalents to **UIC-3 B5S/B7A/Q8C** and triggers dramatic framework shifts (Figure 7). Like with Ag^+, multiple Hg^{2+} ions bind to C8, and another equivalent also coordinates to the bipyridyl unit. However, unlike with Ag^+, a Hg^{2+} ion also coordinates with the carboxamide oxygen of BPH (perhaps due to the higher Lewis acidity of Hg^{2+}), creating an S−Hg−O linkage that results in a large framework slip, similar to that observed in **UIC 3.1**. Most importantly, the examples of coordination of **UIC-3 B5S/B7A/Q8C** with Ag^+ and Hg^{2+} demonstrate the remarkable flexibility and dynamics possible with the peptide-based frameworks. By possessing flexibility, the peptide framework can morph to optimize its interactions with metals.

In **UIC-4**, the C7−NIO1 pair (vide supra) has the correct geometry for a S, N bidentate metal-binding pocket. Bidentate binding could allow stronger metal coordination via the chelate effect, and examples of this chelation in frameworks are rare. Indeed, **UIC-4** binds Pb^{2+} using both C7 and NIO1 in a bidentate mode (Pb···S distance of 2.69 Å and Pb···N distance of 2.60 Å), and the bond lengths suggest a thiolate−Pb interaction. One bidentate acetate is coordinated to Pb^{2+} in **UIC-4**, and overall, the geometry is a hemidirected tetrahedral that is typical for Pb^{2+} (due to its $6s^2$ lone pair).[55] Unusually, Hg^{2+} (0.1 M solution), despite its strong thiophilicity, does not bind to **UIC-4** (as determined by SC-XRD, Figure 7), and a closer examination at the space-filling model of **UIC-4** shows that the tight crevice restricts ligand binding to one coordination hemisphere (Figure S31), consequently only accommodating low-coordinate hemidirected geometries typical of Pb^{2+} (other geometries such as tetrahedral, square planar, or trigonal planar would clash with the surroundings). Hence, **UIC-4** utilizes sterics to selectively capture Pb^{2+}. The precedent for the selective binding of a hemidirected Pb^{2+} geometry is found in a transcription regulator, PbrR691, of bacteria adapted to environments rich in toxic metals.[56]

Given the ability of **UIC-3 B5S/B7A/Q8C** to bind various metals, we quantified its capture capabilities using inductively coupled plasma-mass spectrometry (ICP−MS) (Figure 8).

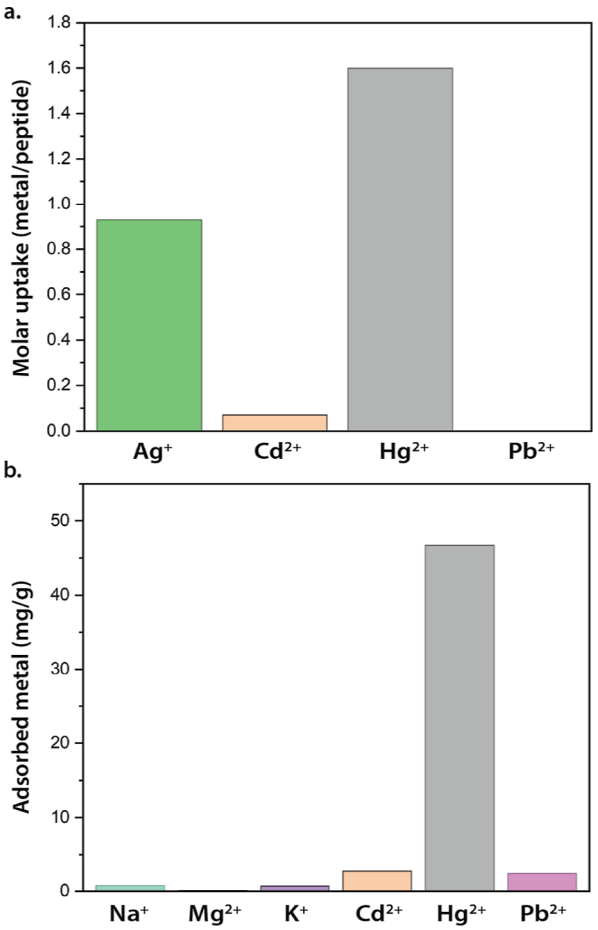

Figure 8. (a) Single-component uptake of metal ions by **UIC-3 B5S/B7A/Q8C** from 0.005 M aqueous solution. Uptake is less than that observed by SC-XRD due to the more dilute metal concentration. (b) Mixed metal uptake by **UIC-3 B5S/B7A/Q8C**.

Crystals were soaked in dilute aqueous metal ion solutions (0.005 M; volumes adjusted to have molar equivalents equal to 90% of the maximum binding stoichiometry derived from SC-XRD) for 24 h. The relative binding affinity was found to be: $Cd^{2+} \sim Pb^{2+} \ll Ag^+ < Hg^+$. The softest ions, Ag^+ and Hg^{2+}, are highly thiophilic and demonstrate the greatest adsorption. Note that the concentration of metal used in this soaking experiment is 20 times less than that for SC-XRD, resulting in less adsorption. As a proof-of-concept for demonstrating reusability, we regenerated **UIC-3 B5S/B7A/Q8C** after Hg^{2+} capture with 0.01 M HCl (pH 2), and showed that the recycled material remains 71% active (Table S22). Lastly, we showed that this material very selectively removes Hg^{2+} from a mixture of common ions in water (Figure 8b).

https://doi.org/10.1021/jacs.3c03645
J. Am. Chem. Soc. 2023, 145, 19588−19600

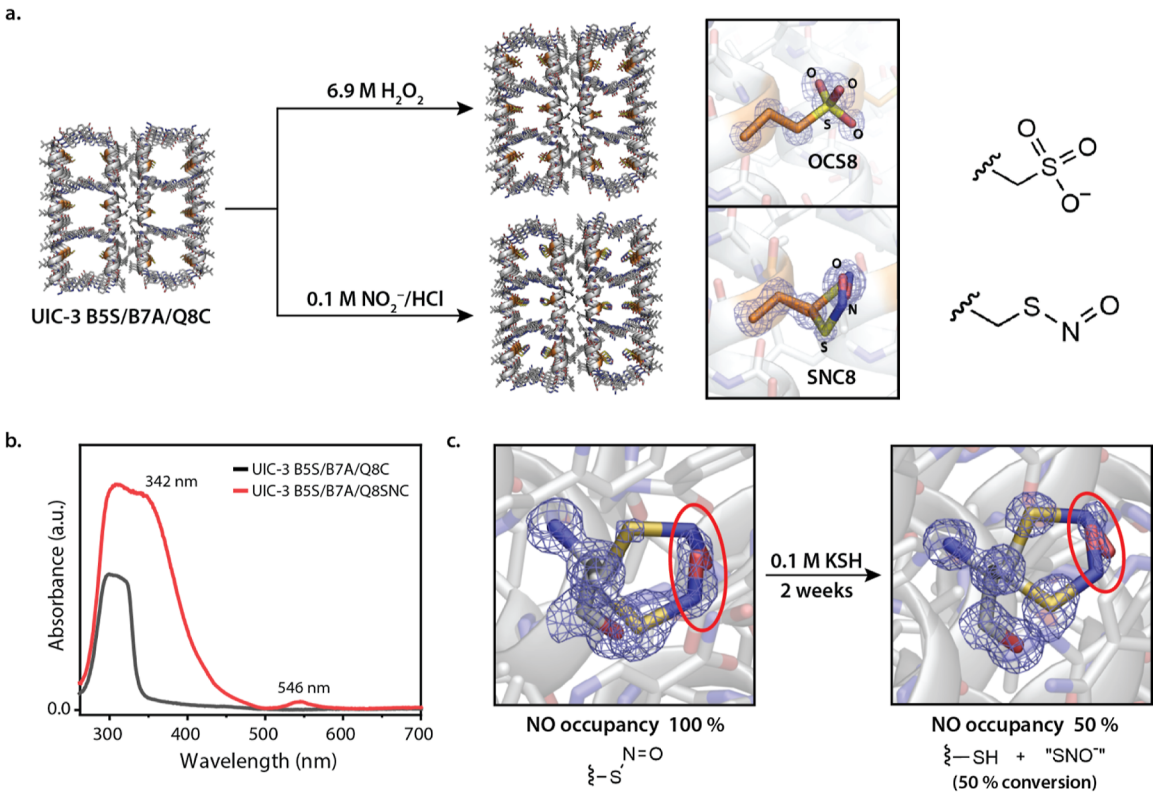

Figure 9. X-ray crystal structures from single-crystal-to-single-crystal redox reactions of thiol-containing frameworks. (a) Oxidation of **UIC-3 B5S/B7A/Q8C.** (b) single-crystal UV−vis spectra of **UIC-3 B5S/B7A/Q8SNC** (red), showing characteristic peaks of S-nitrosothiols. (c) Partial release of a formal NO^+ group by SH^-, regenerating **UIC-3 B5S/B7A/Q8C** ($2F_o - F_c$ map at 1.2 σ).

Redox Reactivity. The range of oxidation states available to sulfur enables the conversion of thiols to other useful functional groups by oxidation reactions (Figure 9). For example, sulfonic acids are potent acids ($pK_a < 0$), and known materials bearing this functional group have widespread uses as ion-exchange membranes,[57] proton-conducting polymers,[58,59] and solid-state catalysts.[60,61] Furthermore, oxidation of Cys by reactive oxygen and nitrogen species is central in biological pathways, and therefore, the sulfur sites of these materials provide a scaffold to better understand the nature of these reactive species.

Immersion of **UIC-3 B5S/B7A/Q8C** crystals in 30% H_2O_2 for 1 week showed no sign of physical degradation. SC-XRD and liquid chromatography mass spectrometry revealed that the thiol group of Cys had fully oxidized to a sulfonic acid group (cysteic acid; three-letter code, OCS). By crystallography, it is unclear if the sulfonate is protonated, but it is certain that NIO has remained neutral due to the preservation of the H bond involving the pyridyl N atom. This leaves the most likely site for protonation as the N atoms on BPH, which are expected to have a pK_a value of ∼0.85.[53] Thus, we demonstrated oxidative conversion of the thiol framework into a chiral solid-state strong acid, which may have future applications in catalysis.

Additionally, we pursued the formation and stabilization of nitrosothiol (RSNO) groups—key species in the signaling and delivery of nitric oxide in biology—by the rigid framework. Small-molecule nitrosothiols rapidly degrade thermally or photochemically into disulfides with the expulsion of NO, limiting their use as therapeutics or in biomedical applications,[62] and so, a long-standing goal is to create macromolecules that prolong the release of NO. Crystals of **UIC-3 B5S/B7A/Q8C** were soaked in a 1:1 mixture of $NaNO_2$ and HCl (0.1 M), turning them into a pale pink color typical of nitrosothiols, with characteristic electronic adsorption bands at 342 and 546 nm (Figure 9b).[62] The color remained stable for more than 1 week, after which the crystals were examined by SC-XRD. The structure revealed complete conversion to an −SNO unit (three-letter code is SNC; S−N length of 1.70 Å and N−O length of 1.57 Å). We next examined whether the NO moiety could be released from the framework as a proof-of-principle for a NO delivery platform. Crystals of **UIC-3 B5S/B7A/Q8SNC** were soaked with hydrosulfide (SH^-), a biological species that releases NO from nitrosothiols.[63] After 2 weeks, SC-XRD revealed a significantly reduced electron density (from the $2F_o - F$ map), where the NO group should be with refinement yielding an occupancy of 50% (Figure 9c). This indicates that this material releases NO with an approximate half-life of 2 weeks, demonstrating its potential as a biocompatible NO slow-release agent, which has important applications in cardiovascular disease, wound healing, bacterial infections, and cancer.[64,65]

CONCLUSIONS AND OUTLOOK

By employing a noncovalent peptide assembly, we have developed a general method to overcome long-standing challenges associated with introducing useful thiol groups into crystalline porous materials. The thiol-containing peptide frameworks can leverage the highly specific steric and electronic environments encoded by the sequence to selectively bind a variety of metal ions, including highly toxic aqueous contaminants, demonstrating that these could be further developed into efficient sorbents. Interestingly, Hg^{2+} coordination induces large conformational changes, a feature reminiscent of metal-binding proteins like calmodulin and lanmodulin[66,67]

https://doi.org/10.1021/jacs.3c03645
J. Am. Chem. Soc. 2023, 145, 19588−19600

that could be leveraged in future designs to enhance selectivity. Furthermore, the thiol groups can be converted into other useful moieties such as sulfonic acid and nitrosothiol; in particular, the nitrosothiol-containing framework is potentially a biocompatible, metal-free, slow-release nitric oxide platform to complement inorganic-based frameworks.[68−70]

The mild noncovalent assembly conditions—owing to the use of π-stacking, hydrophobic interactions, H bonding, and other weak forces—are essential for tolerating the sensitive thiol group, and this strategy creates future opportunities for engineering frameworks possessing more reactive pore environments. The reversibility of the noncovalent assembly significantly facilitates the growth of single crystals for characterization by SC-XRD, which was essential for rationalizing several unexpected properties of these frameworks. We anticipate that materials made using this reported strategy will possess well-defined structure−function relationships that expedite the iterative cycle of design and characterization. Though the reliance on weak forces can result in flexible structures lacking permanent porosity typically desired for gas sorption, these frameworks may be well suited for separations and catalytic applications in liquid media.

Notably, we employed a combination of rational and exploratory-based methods to discover the peptide frameworks in this report. While high-resolution crystal structures can suggest reasonable sites for engineering, the complex cooperation of weak noncovalent interactions comprising the architecture of these materials enables them to readily morph into unexpected structures even with simple sequence variations or binding events. Unpredictability hinders pure rational design, but it also allows for the potential to discover novel and fundamentally interesting solutions that further the understanding of peptide self-assembly. Given the number of variable sites already existing in the reported peptides and future opportunities to increase the sequence length, there are an exponential number of pathways toward new frameworks by rational and high-throughput approaches to obtain highly effective and functional materials.

■ ASSOCIATED CONTENT

Supporting Information

The Supporting Information is available free of charge at https://pubs.acs.org/doi/10.1021/jacs.3c03645.

Experimental synthetic, spectroscopic, and crystallographic details (PDF)

Model of **UIC-5.1C5B** (CIF)

X-ray crystallographic data for **UIC-2**, **UIC-2 B5C**, **UIC-2 C7H**, **UIC-3**, **UIC-3 B5C/B7C**, **UIC-3 B5S/B7A/Q8C**, **UIC-3 B5S/B7A/Q8C + Pb^{2+}**, **UIC-3 B5S/B7A/Q8C + Cd^{2+}**, **UIC-3 B5S/B7A/Q8C + Ag^{+}**, **UIC-3 B5S/B7A/Q8C + Hg^{2+}**, **UIC-3 B5S/B7A/Q8OCS**, **UIC-3 B5S/B7A/Q8SNC**, **UIC-3 B5S/B7A/Q8SNC + SH^{-}**,**UIC-3.1**, **UIC-3.1 Q8C**, **UIC-4**, **UIC-4 + Pb^{2+}**, **UIC-4 NIO1BEZ**, **UIC-5**, and **UIC-5.1** deposited in the Protein Data Bank with codes 8GK9, 8GL0, 8GKX, 8GK1, 8GL4, 8GBA, 8GB9, 8GKB, 8GK2, 8SW2, 8GBH, 8GL5, 8SY4, 8GD8, 8GJ7, 8GBO, 8GBM, 8GIV, 8GD6, and 8GBI, respectively

■ AUTHOR INFORMATION

Corresponding Author

Andy I. Nguyen − *Department of Chemistry, University of Illinois Chicago, Chicago, Illinois 60607, United States;* orcid.org/0000-0003-4137-6453; Email: andyn@uic.edu

Authors

Selina S. Hess − *Department of Chemistry, University of Illinois Chicago, Chicago, Illinois 60607, United States*

Francesco Coppola − *Department of Chemistry, University of Illinois Chicago, Chicago, Illinois 60607, United States;* orcid.org/0000-0002-2429-204X

Viet Thuc Dang − *Department of Chemistry, University of Illinois Chicago, Chicago, Illinois 60607, United States*

Phuong Nguyen Tran − *Department of Chemistry, University of Illinois Chicago, Chicago, Illinois 60607, United States*

Philip J. Mickel − *Department of Chemistry, University of Illinois Chicago, Chicago, Illinois 60607, United States*

Julia Oktawiec − *Department of Chemistry, Northwestern University, Evanston, Illinois 60208, United States;* orcid.org/0000-0002-2895-3327

Zhong Ren − *Department of Chemistry, University of Illinois Chicago, Chicago, Illinois 60607, United States;* orcid.org/0000-0001-7098-3127

Petr Král − *Department of Chemistry, University of Illinois Chicago, Chicago, Illinois 60607, United States;* orcid.org/0000-0003-2992-9027

Complete contact information is available at: https://pubs.acs.org/10.1021/jacs.3c03645

Notes

The authors declare no competing financial interest.

■ ACKNOWLEDGMENTS

This research was supported by start-up funds from the University of Illinois at Chicago. A.I.N. and S.S.H. were supported by the American Chemical Society Petroleum Research Fund (62285-DNI). P.N.T. was supported by the UIC Honors College Research grant. J.O. was supported by the National Institute of General Medical Sciences under award F32GM143925. F.C. and P.K. were supported by the National Science Foundation (NSF DMR 2212123). This research used resources of the Advanced Photon Source, a U.S. Department of Energy (DOE) Office of Science User Facility operated for the DOE Office of Science by Argonne National Laboratory under contract no. DE-AC02-06CH11357. Use of the LS-CAT Sector 21 was supported by the Michigan Economic Development Corporation and the Michigan Technology Tri-Corridor (grant 085P1000817). Data were collected at the Life Sciences Collaborative Access Team beamline 21-ID-D, 21-ID-F, and 21-ID-G at the Advanced Photon Source, Argonne National Laboratory. The authors thank Dr. Charlotte L. Stern and the IMSERC Crystallography facility at Northwestern University, which has received support from the Soft and Hybrid Nanotechnology Experimental (SHyNE) Resource (NSF ECCS-2025633), and Northwestern University. Metal analysis was performed at the Northwestern University. The authors thank Rebecca A. Sponenburg and the Quantitative Bio-element Imaging Center, which is generously supported by NASA Ames Research Center NNA06CB93G.

REFERENCES

(1) Levin, A.; Hakala, T. A.; Schnaider, L.; Bernardes, G. J. L.; Gazit, E.; Knowles, T. P. J. Biomimetic Peptide Self-Assembly for Functional Materials. *Nat. Rev. Chem* **2020**, *4*, 615−634.

(2) Zou, R.; Wang, Q.; Wu, J.; Wu, J.; Schmuck, C.; Tian, H. Peptide Self-Assembly Triggered by Metal Ions. *Chem. Soc. Rev.* **2015**, *44*, 5200−5219.

(3) Hendricks, M. P.; Sato, K.; Palmer, L. C.; Stupp, S. I. Supramolecular Assembly of Peptide Amphiphiles. *Acc. Chem. Res.* **2017**, *50*, 2440−2448.

(4) Dong, J.; Liu, Y.; Cui, Y. Artificial Metal−Peptide Assemblies: Bioinspired Assembly of Peptides and Metals through Space and across Length Scales. *J. Am. Chem. Soc.* **2021**, *143*, 17316−17336.

(5) Collins, J. M.; Porter, K. A.; Singh, S. K.; Vanier, G. S. High-Efficiency Solid Phase Peptide Synthesis (HE-SPPS). *Org. Lett.* **2014**, *16*, 940−943.

(6) Mijalis, A. J.; Thomas, D. A.; Simon, M. D.; Adamo, A.; Beaumont, R.; Jensen, K. F.; Pentelute, B. L. A Fully Automated Flow-Based Approach for Accelerated Peptide Synthesis. *Nat. Chem. Biol.* **2017**, *13*, 464−466.

(7) Katsoulidis, A. P.; Antypov, D.; Whitehead, G. F. S.; Carrington, E. J.; Adams, D. J.; Berry, N. G.; Darling, G. R.; Dyer, M. S.; Rosseinsky, M. J. Chemical Control of Structure and Guest Uptake by a Conformationally Mobile Porous Material. *Nature* **2019**, *565*, 213−217.

(8) Lewandowska, U.; Zajaczkowski, W.; Corra, S.; Tanabe, J.; Borrmann, R.; Benetti, E. M.; Stappert, S.; Watanabe, K.; Ochs, N. A. K.; Schaeublin, R.; Li, C.; Yashima, E.; Pisula, W.; Müllen, K.; Wennemers, H. A Triaxial Supramolecular Weave. *Nat. Chem.* **2017**, *9*, 1068−1072.

(9) Schnitzer, T.; Paenurk, E.; Trapp, N.; Gershoni-Poranne, R.; Wennemers, H. Peptide−Metal Frameworks with Metal Strings Guided by Dispersion Interactions. *J. Am. Chem. Soc.* **2021**, *143*, 644−648.

(10) Misra, R.; Saseendran, A.; Dey, S.; Gopi, H. N. Metal-Helix Frameworks from Short Hybrid Peptide Foldamers. *Angew. Chem. Int. Ed.* **2019**, *58*, 2215−2255.

(11) Saito, A.; Sawada, T.; Fujita, M. X-Ray Crystallographic Observation of Chiral Transformations within a Metal−Peptide Pore. *Angew. Chem., Int. Ed.* **2020**, *59*, 20367−20370.

(12) Heinz-Kunert, S. L.; Pandya, A.; Dang, V. T.; Tran, P. N.; Ghosh, S.; McElheny, D.; Santarsiero, B. D.; Ren, Z.; Nguyen, A. I. Assembly of π-Stacking Helical Peptides into a Porous and Multivariable Proteomimetic Framework. *J. Am. Chem. Soc.* **2022**, *144*, 7001−7009.

(13) Navarro-Sánchez, J.; Argente-García, A. I.; Moliner-Martínez, Y.; Roca-Sanjuán, D.; Antypov, D.; Campíns-Falcó, P.; Rosseinsky, M. J.; Martí-Gastaldo, C. Peptide Metal−Organic Frameworks for Enantioselective Separation of Chiral Drugs. *J. Am. Chem. Soc.* **2017**, *139*, 4294−4297.

(14) Chen, Y.; Guerin, S.; Yuan, H.; O'Donnell, J.; Xue, B.; Cazade, P.-A.; Haq, E. U.; Shimon, L. J. W.; Rencus-Lazar, S.; Tofail, S. A. M.; Cao, Y.; Thompson, D.; Yang, R.; Gazit, E. Guest Molecule-Mediated Energy Harvesting in a Conformationally Sensitive Peptide−Metal Organic Framework. *J. Am. Chem. Soc.* **2022**, *144*, 3468−3476.

(15) Martí-Gastaldo, C.; Antypov, D.; Warren, J. E.; Briggs, M. E.; Chater, P. A.; Wiper, P. V.; Miller, G. J.; Khimyak, Y. Z.; Darling, G. R.; Berry, N. G.; Rosseinsky, M. J. Side-Chain Control of Porosity Closure in Single- and Multiple-Peptide-Based Porous Materials by Cooperative Folding. *Nat. Chem.* **2014**, *6*, 343−351.

(16) Rabone, J.; Yue, Y.-F.; Chong, S. Y.; Stylianou, K. C.; Bacsa, J.; Bradshaw, D.; Darling, G. R.; Berry, N. G.; Khimyak, Y. Z.; Ganin, A. Y.; Wiper, P.; Claridge, J. B.; Rosseinsky, M. J. An Adaptable Peptide-Based Porous Material. *Science* **2010**, *329*, 1053−1057.

(17) Fletcher, J. M.; Harniman, R. L.; Barnes, F. R. H.; Boyle, A. L.; Collins, A.; Mantell, J.; Sharp, T. H.; Antognozzi, M.; Booth, P. J.; Linden, N.; Miles, M. J.; Sessions, R. B.; Verkade, P.; Woolfson, D. N. Self-Assembling Cages from Coiled-Coil Peptide Modules. *Science* **2013**, *340*, 595−599.

(18) Hill, R. B.; Raleigh, D. P.; Lombardi, A.; DeGrado, W. F. De Novo Design of Helical Bundles as Models for Understanding Protein Folding and Function. *Acc. Chem. Res.* **2000**, *33*, 745−754.

(19) Truebestein, L.; Leonard, T. A. Coiled-Coils: The Long and Short of It. *BioEssays* **2016**, *38*, 903−916.

(20) LoPachin, R. M.; Gavin, T. Reactions of Electrophiles with Nucleophilic Thiolate Sites: Relevance to Pathophysiological Mechanisms and Remediation. *Free Radic. Res.* **2016**, *50*, 195−205.

(21) Paulsen, C. E.; Carroll, K. S. Cysteine-Mediated Redox Signaling: Chemistry, Biology, and Tools for Discovery. *Chem. Rev.* **2013**, *113*, 4633−4679.

(22) Groitl, B.; Jakob, U. Thiol-Based Redox Switches. *Biochim. Biophys. Acta Protein Proteonomics* **2014**, *1844*, 1335−1343.

(23) Antelmann, H.; Helmann, J. D. Thiol-Based Redox Switches and Gene Regulation. *Antioxid. Redox Signaling* **2011**, *14*, 1049−1063.

(24) Orrillo, A. G.; Furlan, R. L. E. Sulfur in Dynamic Covalent Chemistry. *Angew. Chem., Int. Ed.* **2022**, *61*, No. e202201168.

(25) Pearson, R. G. Hard and Soft Acids and Bases. *J. Am. Chem. Soc.* **1963**, *85*, 3533−3539.

(26) Turk, B. Targeting Proteases: Successes, Failures and Future Prospects. *Nat. Rev. Drug Discovery* **2006**, *5*, 785−799.

(27) Nordlund, P.; Reichard, P. Ribonucleotide Reductases. *Annu. Rev. Biochem.* **2006**, *75*, 681−706.

(28) Arnér, E. S. J.; Holmgren, A. Physiological Functions of Thioredoxin and Thioredoxin Reductase. *Eur. J. Biochem.* **2000**, *267*, 6102−6109.

(29) Roche, B.; Aussel, L.; Ezraty, B.; Mandin, P.; Py, B.; Barras, F. Iron/Sulfur Proteins Biogenesis in Prokaryotes: Formation, Regulation and Diversity. *Biochim. Biophys. Acta Bioenerg.* **2013**, *1827*, 455−469.

(30) Solomon, E. I.; Szilagyi, R. K.; DeBeer George, S.; Basumallick, L. Electronic Structures of Metal Sites in Proteins and Models: Contributions to Function in Blue Copper Proteins. *Chem. Rev.* **2004**, *104*, 419−458.

(31) Hamer, D. H. Metallothionein. *Annu. Rev. Biochem.* **1986**, *55*, 913−951.

(32) Zanger, U. M.; Schwab, M. Cytochrome P450 Enzymes in Drug Metabolism: Regulation of Gene Expression, Enzyme Activities, and Impact of Genetic Variation. *Pharmacol. Ther.* **2013**, *138*, 103−141.

(33) Denisov, I. G.; Makris, T. M.; Sligar, S. G.; Schlichting, I. Structure and Chemistry of Cytochrome P450. *Chem. Rev.* **2005**, *36*, 2253−2278.

(34) Brandes, N.; Schmitt, S.; Jakob, U. Thiol-Based Redox Switches in Eukaryotic Proteins. *Antioxid. Redox Signaling* **2009**, *11*, 997−1014.

(35) Parvez, S.; Long, M. J. C.; Poganik, J. R.; Aye, Y. Redox Signaling by Reactive Electrophiles and Oxidants. *Chem. Rev.* **2018**, *118*, 8798−8888.

(36) Lowe, A. B. Thiol-Ene "Click" Reactions and Recent Applications in Polymer and Materials Synthesis. *Polym. Chem.* **2010**, *1*, 17−36.

(37) Nair, D. P.; Podgórski, M.; Chatani, S.; Gong, T.; Xi, W.; Fenoli, C. R.; Bowman, C. N. The Thiol-Michael Addition Click Reaction: A Powerful and Widely Used Tool in Materials Chemistry. *Chem. Mater.* **2014**, *26*, 724−744.

(38) Spokoyny, A. M.; Zou, Y.; Ling, J. J.; Yu, H.; Lin, Y.-S.; Pentelute, B. L. A Perfluoroaryl-Cysteine SNAr Chemistry Approach to Unprotected Peptide Stapling. *J. Am. Chem. Soc.* **2013**, *135*, 5946−5949.

(39) Li, B.; Zhang, Y.; Ma, D.; Shi, Z.; Ma, S. Mercury Nano-Trap for Effective and Efficient Removal of Mercury(II) from Aqueous Solution. *Nat. Commun.* **2014**, *5*, 5537.

(40) Li, Y.; Tan, M.; Liu, G.; Si, D.; Chen, N.; Zhou, D. Thiol-Functionalized Metal−Organic Frameworks Embedded with Chelator-Modified Magnetite for High-Efficiency and Recyclable Mercury Removal in Aqueous Solutions. *J. Mater. Chem. A* **2022**, *10*, 6724−6730.

(41) Ji, C.; Ren, Y.; Yu, H.; Hua, M.; Lv, L.; Zhang, W. Highly Efficient and Selective Hg(II) Removal from Water by Thiol-Functionalized MOF-808: Kinetic and Mechanism Study. *Chem. Eng. J.* **2022**, *430*, 132960.

https://doi.org/10.1021/jacs.3c03645
J. Am. Chem. Soc. 2023, 145, 19588−19600

(42) Ke, F.; Jiang, J.; Li, Y.; Liang, J.; Wan, X.; Ko, S. Highly Selective Removal of Hg2+ and Pb2+ by Thiol-Functionalized Fe3O4@metal-Organic Framework Core-Shell Magnetic Microspheres. *Appl. Surf. Sci.* **2017**, *413*, 266−274.
(43) Li, G.-P.; Zhang, K.; Zhang, P.-F.; Liu, W.-N.; Tong, W.-Q.; Hou, L.; Wang, Y.-Y. Thiol-Functionalized Pores via Post-Synthesis Modification in a Metal−Organic Framework with Selective Removal of Hg(II) in Water. *Inorg. Chem.* **2019**, *58*, 3409−3415.
(44) Sun, Q.; Ma, W.; Dan, O.; Li, G.; Yang, Y.; Yan, X.; Su, H.; Lin, Z.; Cai, Z. Thiol Functionalized Covalent Organic Framework for Highly Selective Enrichment and Detection of Mercury by Matrix-Assisted Laser Desorption/Ionization Time-of-Flight Mass Spectrometry. *Analyst* **2021**, *146*, 2991−2997.
(45) Pan, F.; Tong, C.; Wang, Z.; Xu, F.; Wang, X.; Weng, B.; Pan, D.; Zhu, R. Novel Sulfhydryl Functionalized Covalent Organic Frameworks for Ultra-Trace Hg2+ Removal from Aqueous Solution. *J. Mater. Sci. Technol.* **2021**, *93*, 89−95.
(46) Sun, Q.; Aguila, B.; Perman, J.; Earl, L. D.; Abney, C. W.; Cheng, Y.; Wei, H.; Nguyen, N.; Wojtas, L.; Ma, S. Postsynthetically Modified Covalent Organic Frameworks for Efficient and Effective Mercury Removal. *J. Am. Chem. Soc.* **2017**, *139*, 2786−2793.
(47) Yuan, Y.; Yu, J.; Chen, H.; Bang, K.-T.; Pan, D.; Kim, Y. Thiol-Functionalized Zr Metal-Organic Frameworks for Efficient Removal of Fe3+ from Water. *Cell Rep. Phys. Sci.* **2022**, *3*, 100783.
(48) Yee, K.-K.; Reimer, N.; Liu, J.; Cheng, S.-Y.; Yiu, S.-M.; Weber, J.; Stock, N.; Xu, Z. Effective Mercury Sorption by Thiol-Laced Metal−Organic Frameworks: In Strong Acid and the Vapor Phase. *J. Am. Chem. Soc.* **2013**, *135*, 7795−7798.
(49) Li, M.-Q.; Wong, Y.-L.; Lum, T.-S.; Sze-Yin Leung, K.; Lam, P. K. S.; Xu, Z. Dense Thiol Arrays for Metal−Organic Frameworks: Boiling Water Stability, Hg Removal beyond 2 Ppb and Facile Crosslinking. *J. Mater. Chem. A* **2018**, *6*, 14566−14570.
(50) Yang, P.; Shu, Y.; Zhuang, Q.; Li, Y.; Gu, J. A Robust MOF-Based Trap with High-Density Active Alkyl Thiol for the Super-Efficient Capture of Mercury. *Chem. Commun.* **2019**, *55*, 12972−12975.
(51) Cangelosi, V.; Ruckthong, L.; Pecoraro, V. L. 10. Lead(II) Binding in Natural and Artificial Proteins. In *Lead—Its Effects on Environment and Health*; Sigel, A., Sigel, H., Sigel, R. K. O., Eds.; De Gruyter, 2017; pp 271−318.
(52) Rebilly, J.-N.; Gardner, P. W.; Darling, G. R.; Bacsa, J.; Rosseinsky, M. J. Chiral II−VI Semiconductor Nanostructure Superlattices Based on an Amino Acid Ligand. *Inorg. Chem.* **2008**, *47*, 9390−9399.
(53) James, B. R.; Williams, R. J. P. 383. The oxidation−reduction potentials of some copper complexes. *J. Chem. Soc.* **1961**, 2007−2019.
(54) Schmidbaur, H.; Schier, A. Argentophilic Interactions. *Angew. Chem., Int. Ed.* **2015**, *54*, 746−784.
(55) Shimoni-Livny, L.; Glusker, J. P.; Bock, C. W. Lone Pair Functionality in Divalent Lead Compounds. *Inorg. Chem.* **1998**, *37*, 1853−1867.
(56) Huang, S.; Liu, X.; Wang, D.; Chen, W.; Hu, Q.; Wei, T.; Zhou, W.; Gan, J.; Chen, H. Structural Basis for the Selective Pb(II) Recognition of Metalloregulatory Protein PbrR691. *Inorg. Chem.* **2016**, *55*, 12516−12519.
(57) Kusoglu, A.; Weber, A. Z. New Insights into Perfluorinated Sulfonic-Acid Ionomers. *Chem. Rev.* **2017**, *117*, 987−1104.
(58) Yoshimura, K.; Iwasaki, K. Aromatic Polymer with Pendant Perfluoroalkyl Sulfonic Acid for Fuel Cell Applications. *Macromolecules* **2009**, *42*, 9302−9306.
(59) Kreuer, K. D. On the Development of Proton Conducting Polymer Membranes for Hydrogen and Methanol Fuel Cells. *J. Membr. Sci.* **2001**, *185*, 29−39.
(60) Morales, G.; Athens, G.; Chmelka, B.; Vangrieken, R.; Melero, J. Aqueous-Sensitive Reaction Sites in Sulfonic Acid-Functionalized Mesoporous Silicas. *J. Catal.* **2008**, *254*, 205−217.
(61) Zhang, X.; Zhao, Y.; Xu, S.; Yang, Y.; Liu, J.; Wei, Y.; Yang, Q. Polystyrene Sulphonic Acid Resins with Enhanced Acid Strength via Macromolecular Self-Assembly within Confined Nanospace. *Nat. Commun.* **2014**, *5*, 3170.
(62) Marcolongo, J. P.; Zeida, A.; Slep, L. D.; Olabe, J. A. Thionitrous Acid/Thionitrite and Perthionitrite Intermediates in the "Crosstalk" of NO and H_2S. In *Advances in Inorganic Chemistry*; van Eldik, R., Hubbard, C. D., Eds.; Inorganic Reaction Mechanisms; Academic Press, 2017; Vol. *70*, Chapter 7, pp 277−309.
(63) Kolluru, G. K.; Shen, X.; Kevil, C. G. A Tale of Two Gases: NO and H2S, Foes or Friends for Life? *Redox Biol.* **2013**, *1*, 313−318.
(64) Riccio, D. A.; Schoenfisch, M. H. Nitric Oxide Release: Part I. Macromolecular Scaffolds. *Chem. Soc. Rev.* **2012**, *41*, 3731.
(65) Carpenter, A. W.; Schoenfisch, M. H. Nitric Oxide Release: Part II. Therapeutic Applications. *Chem. Soc. Rev.* **2012**, *41*, 3742.
(66) Finn, B. E.; Evenäs, J.; Drakenberg, T.; Waltho, J. P.; Thulin, E.; Forsén, S. Calcium-Induced Structural Changes and Domain Autonomy in Calmodulin. *Nat. Struct. Biol.* **1995**, *2*, 777−783.
(67) Mattocks, J. A.; Jung, J. J.; Lin, C.-Y.; Dong, Z.; Yennawar, N. H.; Featherston, E. R.; Kang-Yun, C. S.; Hamilton, T. A.; Park, D. M.; Boal, A. K.; Cotruvo, J. A. Enhanced Rare-Earth Separation with a Metal-Sensitive Lanmodulin Dimer. *Nature* **2023**, *618*, 87−93.
(68) Bloch, E. D.; Queen, W. L.; Chavan, S.; Wheatley, P. S.; Zadrozny, J. M.; Morris, R.; Brown, C. M.; Lamberti, C.; Bordiga, S.; Long, J. R. Gradual Release of Strongly Bound Nitric Oxide from Fe2(NO)2(Dobdc). *J. Am. Chem. Soc.* **2015**, *137*, 3466−3469.
(69) Wheatley, P. S.; Butler, A. R.; Crane, M. S.; Fox, S.; Xiao, B.; Rossi, A. G.; Megson, I. L.; Morris, R. E. NO-Releasing Zeolites and Their Antithrombotic Properties. *J. Am. Chem. Soc.* **2006**, *128*, 502−509.
(70) Xiao, B.; Wheatley, P. S.; Zhao, X.; Fletcher, A. J.; Fox, S.; Rossi, A. G.; Megson, I. L.; Bordiga, S.; Regli, L.; Thomas, K. M.; Morris, R. E. High-Capacity Hydrogen and Nitric Oxide Adsorption and Storage in a Metal−Organic Framework. *J. Am. Chem. Soc.* **2007**, *129*, 1203−1209.

https://doi.org/10.1021/jacs.3c03645
J. Am. Chem. Soc. 2023, 145, 19588−19600